Anisotropic self-assemblies of magnetic nanoparticles: experimental evidence of low-field deviation from the linear response theory and empirical model

Irene Andreu,[#,†] Ainhoa Urtizberea,[⊥] and Eva Natividad[#,]*

[#]Instituto de Ciencia de Materiales de Aragón (ICMA), CSIC - Universidad de Zaragoza, Campus Río Ebro, María de Luna 3, 50018 Zaragoza, Spain

[†]RI Consortium of Nanoscience and Nanotechnology and Department of Chemical Engineering, University of Rhode Island , Kingston, Rhode Island, 02881, USA

[⊥]Centro Universitario de la Defensa, Carretera de Huesca, s/n, 50090 Zaragoza, Spain

Address correspondence to: evanat@unizar.es.

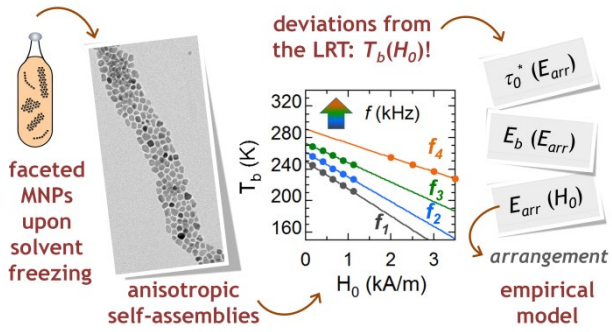

KEYWORDS: magnetic nanoparticles, ac-susceptibility, specific absorption rate, assemblies, magnetic interactions, collective effects, magnetic hyperthermia.

ABSTRACT: The heating ability upon application of an alternating magnetic field of a system of monodisperse and non-interacting superparamagnetic nanoparticles is described by the linear response theory. But in real applications, nanoparticle systems are rarely monodisperse or non-interacting, and predicting their heating ability is challenging, since it requires considering single-particle, interparticle and collective effects. Herein we give experimental evidence of a collective effect that originates a deviation from the linear response theory in self-assembled anisotropic arrangements. This effect allows tuning Néel relaxation times and, in turn, blocking temperatures, just varying the alternating magnetic field amplitude. The analysis of the source magnetic and magnetothermal data leads to the development of an empirical model describing the modified Néel relaxation times in term of characteristic parameters, whose physical interpretation is discussed. As a result, the dependency of Néel relaxation time on the magnetic field amplitude is assigned to a strong interaction energy contribution created locally by the ordered anisotropic assemblies. The reduction of this energy upon application of higher magnetic fields is related to the loss of preferred orientation of the magnetic moment of nanoparticles within assemblies. Remarkably, this energy contribution does not depend on particle volume, so it does not contribute to widen the energy barrier distribution of the assemblies, avoiding this detrimental effect of magnetic interactions, and contributing to an excellent heating ability. This work thus provides an analytical framework to analyze or predict the magnetic behavior and heating ability of superparamagnetic nanoparticles displaying collective effects.

Magnetic nanoparticles (MNPs) are multifunctional materials used in many fields of science and technology.[1] An interesting functionality of MNPs is their ability to convert electromagnetic energy (from an alternating magnetic field, AMF) into heat.

This conversion happens because the applied field, $H(t)$, induces a delayed reversal of the MNP magnetization, $M(t)$. The *M(H)* evolution under an AMF describes thus a hysteresis loop whose area accounts for the heat dissipated per field cycle. This functionality is being mainly exploited in hyperthermia cancer treatment[2] and in heat-assisted drug release[3] although it can be also applied to other biomedical issues (*e.g.* fungus eradication[4] or Alzheimer's disease[5]) as well as to the development of smart materials (*e.g.* shape-memory materials[6] or catalysts[7]).

For *in vivo* applications, the composition of magnetic nanomaterials is restricted to iron oxides (maghemite and magnetite) due to their reduced toxicity compared to the alternatives.[8] Additionally, the AMF parameters are limited to certain values of amplitude, H_0, and frequency, f, to avoid heating of unwanted areas and interference with biological electromagnetic signals.[9] This limitation depends on the body area. For example, for a typical frequency of 100 kHz, clinical trials conclude that H_0 values are limited to 3 - 5 kA/m in the pelvic region or 8.5 kA/m in the upper thorax.[10] Obviously, the higher heating ability of MNPs for these field ranges, the lower dose must be used, and the lower toxicity is induced. For this reason, MNPs with sizes next to the limit between the superparamagnetic (SPM) and the ferro/ferromagnetic (FM) behavior are best candidates, since they show optimum dissipation ability at these low fields.[11]

Rosensweig's model of superparamagnetism[12] predicts that, when H_0 is small enough to fulfill the requirements of the linear response theory (LRT), the out-of-phase ac susceptibility (χ'') and the heat power released per mass unit of MNPs (specific absorption rate, SAR) are proportional. Accordingly, both magnitudes share the same dependence with temperature. The LRT implies that the MNP magnetization is linear with the applied field. Thus χ'' is independent of H_0, although dependent on f and also on T. $\chi''(T)$ is a function with a maximum (χ''_{max}) that takes place at the so-called blocking temperature (T_b), which delimits the FM ($T < T_b$) and the SPM ($T > T_b$) behavior. When T_b matches the operation temperature (37-45ºC) in magnetic hyperthermia, the heating efficiency of the MNPs is maximum. According to Rosensweig's model, T_b is reached at $2\pi f\tau = 1$, where τ is the relaxation time for magnetization reversal, which is equal to Néel relaxation time (τ_N) for immobilized MNPs (case of MNPs in a tissue). τ_N depends on the energy barrier for magnetization reversal (E_b) and on the temperature. E_b in turn depends on the MNP size (and magnetic anisotropy). This means that, for a given f, and MNP composition, the matching of T_b with operation temperature will take place for a particular MNP size.

The abovementioned Rosensweig's model is strictly valid either for a single MNP or for monodisperse MNP arrangements without interparticle magnetic interactions. However, real MNP self-assemblies are rarely monodisperse or non-interacting, and predicting their heating ability is currently a challenging issue. Size polydispersity generates a distribution of τ_N values, which in turn widen the $\chi''(T)$ function, decrease χ''_{max} and shift T_b.[13] Interparticle magnetic interactions also affect the energy landscape of the system, causing similar and further effects on $\chi''(T)$.[14-15] As a consequence, $\chi''(T)$ and SAR(T) functions become unknown, as well as the value of T_b, with direct implications in applications.

The above implies that, either when modeling SAR, or when analyzing experimental SAR data of MNP self-assemblies, individual-particle and inter-particle characteristics must be considered. In addition, in contrast with continuous ferromagnetic materials, exchange coupling does no longer limit the creation of magnetic configurations and long domains in MNPs self-assemblies, and dipolar interactions can induce collective magnetic properties in close-packed structures (case of MNPs in cell vesicles) dependent on the particular MNPs arrangement.[16-20] This arrangement depends on, among other properties, MNP shape. Cubic or faceted MNPs tend to self-organize face-to-face, leading preferably to chains or columns with ferromagnetic order.[19-21] This is contrary to spherical MNPs that usually self-assemble in hexagonal packing. Eventually, these trends are tuned by MNP size dispersity. In sum, the assumption of a randomly oriented system with dipolar interactions[22] is not applicable to all arrangements, and usually-neglected collective effects must be appraised.[19,23-24]

Herein, we provide experimental evidence of how collective behavior may also bring about deviations from the linear response theory: the blocking temperature can vary with H_0 even at very low H_0 values, providing another variable to control T_b. Combining magnetic measurements with SAR(T) data[25] from our unique characterization setup,[26] we are able to cover a wide range of f and H_0 values, and also to sweep in E_b just changing H_0. The analysis of these data provides an empirical model for τ_N with several characteristic parameters, whose physical meaning is interpreted through reported theoretical outputs. This model includes collective effects and explains the excellent heating ability observed in anisotropic MNPs self-assemblies. The present work provides a framework to consider the arrangement of the MNPs when comparing their heating ability and magnetic properties with theoretical predictions.

Framework for data analysis. Returning to Rosensweig's model (see SI for a more detailed description) $\chi''(T)$ and SAR(T) in the LRT are proportional as,

$$SAR = \frac{\pi\mu_0}{\rho_{MNP}} f H_0^2 \chi'' \qquad (1)$$

where $\mu_0 = 4\pi\text{x}10^{-7}$ T·m/A is the permeability of free space and ρ_{MNP} is the density of the magnetic material. In the LRT χ'' is independent of H_0, although dependent on f,

$$\chi'' = \chi_0 \cdot \frac{2\pi f\tau}{1+(2\pi f\tau)^2} \qquad (2)$$

and also on T through both the static susceptibility (χ_0) and τ ($\equiv \tau_N$ on immobilized MNPs). The simplified expression for τ_N follows the Arrhenius law,

$$\tau \equiv \tau_N = \tau_0 exp\left(\frac{E_b \equiv E_{b0}}{k_B T}\right) \qquad (3)$$

where τ_0 is the attempt time, $\tau_0 = 10^{-8} - 10^{-10}$ s, and E_{b0} is the barrier energy for magnetization reversal in absence of interactions (*i.e.*, E_{b0} is only created by the anisotropy energy of the MNP). These dependencies are enclosed in the scaling variable $-T\cdot\ln(2\pi f\tau_0)$.[27] Accordingly, the $\chi''(T)$ *vs.* $-T\cdot\ln(2\pi f\tau_0)$ curves for different AMF frequencies should collapse if the χ''

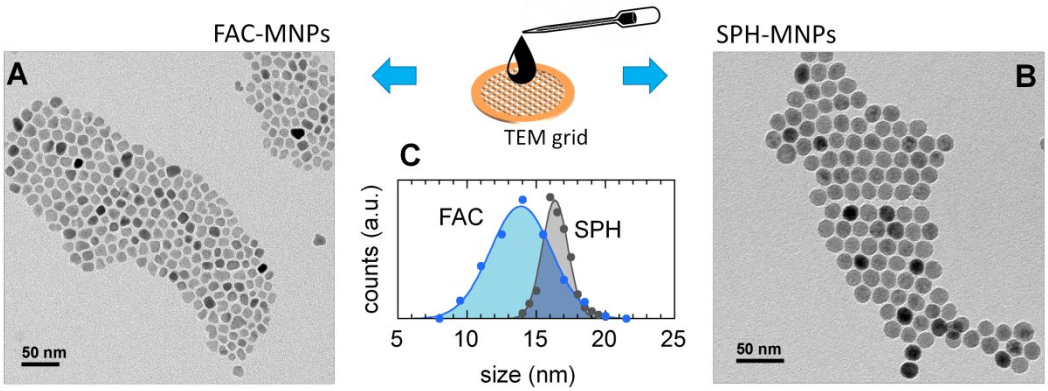

Figure1. TEM images of faceted (A) and spherical (B) magnetic nanoparticles, obtained by drop casting the starting organic MNP suspensions onto TEM grids. C: MNP size distributions fitted to normal functions.

height is normalized to account for different χ_0 values ($\chi''_{max} = \chi_0/2$). Given that χ'' and SAR are proportional, $-T\cdot\ln(2\pi f\tau_0)$ should also act as scaling variable for SAR(T) curves with different AMF frequencies. Eventually, this variable should be able to make SAR(T) collapse with $\chi''(T)$ functions after the adequate height normalization.

Moreover, $E_{b0} = K_{eff}\cdot V$, where K_{eff} is the effective magnetic anisotropy constant and V is the MNP volume. Accordingly, the most evident origin of E_b distribution in a MNP assembly is the MNP size polydispersity. K_{eff} stands for the sum of several contributions, such as magnetocrystalline, surface or shape anisotropies. Surface anisotropy, relevant for small-sized MNPs, depends in turn on V. The shape anisotropy term points that shape may be another source of E_b distribution. In addition, interparticle interactions can modify the magnetic landscape experienced by individual MNPs. Often in these cases E_b is described with an apparent anisotropy constant (K_{app}) as $E_b = K_{app}\cdot V$. K_{app} can take values very different from those of K_{eff}. It has been shown that interparticle dipolar interactions in disperse MNP systems can either generate small perturbations to E_{b0} or fully govern E_b, depending on the K_{eff} of individual MNPs and/or the interaction strength.[28,29] If the system involves some MNP agglomeration, then it can display a new distribution of K_{app} values related to the size of the aggregates.[13] Nevertheless, it is still possible to describe the relaxation time of such assemblies using equation 3 with modified attempt times and/or energy barriers. Therefore, even in the case of magnetic interactions, $\chi''(T)$ and SAR(T) should collapse when plotted against $T\cdot\ln(2\pi f\tau_0)$.[13,30] Based on these findings, the experimental data herein were analyzed in the framework of this data collapse.

Faceted and spherical magnetic nanoparticles. Arrangements were prepared using magnetite MNPs with two different morphologies, spherical (**SPH**, which are the SOR-18 from Ocean Nanotech) and faceted (**FAC**, lab-synthetized[31]). SPH MNPs display a very homogeneous shape (see Figure 1), and are highly monodisperse in size, with a mean diameter of 16.4 nm and standard deviation of 0.9 nm (5%). FAC MNPs are polyhedral and more heterogeneous in shape than SPH MNPs, as revealed by TEM in Figure 1. Also, they are more polydisperse, with a mean diameter of 13.9 nm and standard deviation of 2.2 nm (16%). Note that the biggest FAC MNPs are the same size of the average SPH MNPs, but the presence of smaller MNPs (down to 9 nm) reduces the mean diameter of FAC MNPs. The saturation magnetization (see Figure S2) of SPH MNPs is M_s = 330.0 kA/m (63.7 emu/g), appreciably smaller than that of bulk magnetite (~446 kA/m). In contrast, FAC MNPs have a M_S of 420.6 kA/m (81.2 emu/g), only slightly lower than that of bulk magnetite. A reduced M_s is ascribed to the presence of several defects in the crystalline structure of MNPs, leading to a divergence between geometric and magnetic sizes.[32] This divergence would be stronger in spherical than in faceted MNPs, due to a presumably faster MNP growth leading to more defects. With the data above, it is already possible to estimate the maximum H_0 value for which the LRT is valid[11] (according to equation S3). This value depends on T, and it is $H_0 < 14.41\cdot T$ A/m and $H_0 < 18.17\cdot T$ A/m for SPH and FAC, respectively. Therefore, in the temperature range of 200 – 300 K, H_0 values would be below 2.9 – 4.3 kA/m and 3.6 – 5.4 kA/m for SPH and FAC, respectively.

Randomly arranged big clusters. The first selected arrangement was obtained embedding SPH and FAC MNPs into epoxy resin to produce samples **SPH-E** and **FAC-E** (see SI and scheme I in Figure 2). SPH-E and FAC-E have an average concentration of $1.60\cdot10^{-1}$ g/g and $8.16\cdot10^{-2}$ g/g respectively (g of MNPs per gram of sample). However, TEM images (Figure 2) of cross-sections perpendicular to the cylinder axis reveal that the MNP distribution is inhomogeneous. Figure 2 also shows Fast Fourier Transforms (FFTs) of the corresponding TEM images to help evaluate the arrangement of MNPs upon embedding in epoxy resin. SPH-E is mostly formed by disordered big clusters (Figure 2A-B). A few ordered areas displaying three dimensional hexagonal arrangements (Figure 2C) can be discerned. The presence of bright spots in the reciprocal space (Figure 2D) indicates that both the spacing and the orientation of these arrangement are quite homogeneous due to the monodispersity of these MNPs. But given that these areas are scarce, SPH-E can be considered to contain randomly arranged big clusters. FAC-E is also constituted by big clusters that, according to Figure 2F, do not show an overall order. However, the faceted shape of these MNPs promotes the local formation of small chains and 2D structures in the clusters.

In order to detect a possible anisotropy in SPH-E and FAC-E from the magnetic point of view, $M(H)$ measurements were performed on these samples with the applied dc field both parallel and perpendicular to the cylinder axis (Figure S2). In

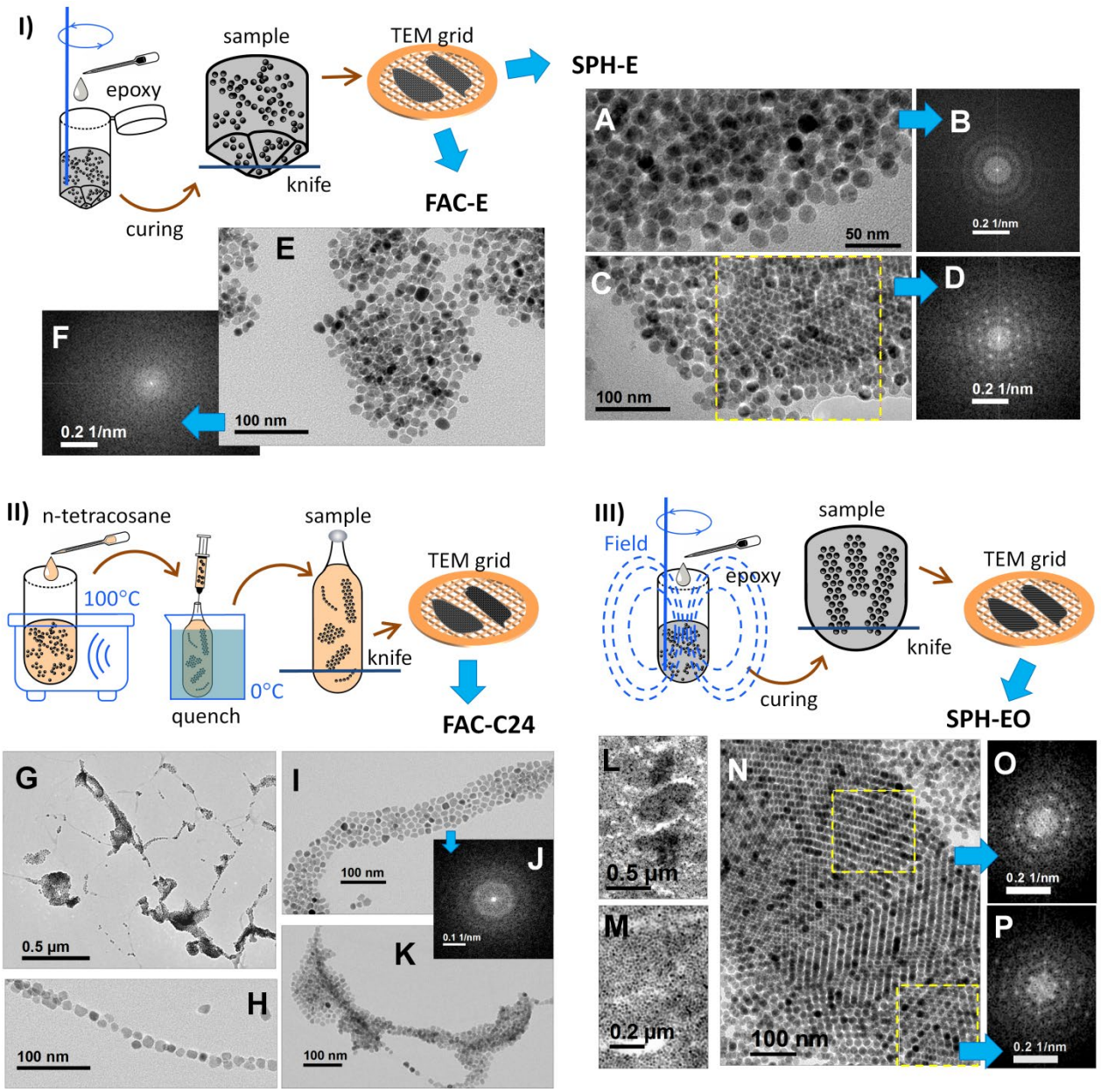

Figure2. Arrangements of FAC and SPH MNPs. **I)** Top-left: scheme illustrating sample preparation and later ultramicrotomy sectioning for TEM observation of samples FAC-E and SPH-E (randomly arranged big clusters of FAC and SPH MNPs). Bottom-left: TEM image (E) and FFT (F) of FAC-E. Right: TEM images (A, C) and FFTs (B, D) of disordered and ordered areas of SPH-E, respectively. **II)** Top: scheme illustrating sample preparation (see experimental section for more details), and afterward ultramicrotomy sectioning for TEM observation, of sample FAC-C24 (self-assembly upon matrix solidification of FAC MNPs). Bottom: cross-section TEM images of FAC-C24, revealing random orientation of arrangements (G), chains (H), two-dimensional elongated arrangements with hexagonal order (I, together with FFT, J) and clusters surrounded of these and also square arrangements (K). **III)** Top: scheme illustrating sample preparation (see experimental section for more details), and afterward ultramicrotomy sectioning for TEM observation, of sample SPH-EO (magnetic field-assisted arrangement of SPH MNPs). Bottom: cross-section TEM images of SPH-EO, revealing highly-ordered areas (darker zones in L-N) surrounded by more disperse and disordered zones (lighter areas). Highly-ordered areas present domains with different arrangement orientation, according to FFTs (O and P).

both samples there is a slight anisotropy. The perpendicular $M(H)$ is higher than the parallel at low field, up to *ca.* 1500 Oe (119 kA/m). This increment is of 41 % at 50 Oe (4 kA/m) and 25% at 40 Oe (3.2 kA/m), for SPH-E and FAC-E, respectively. Figure S2 also shows zero-field-cooled and field-cooled magnetization curves (ZFC/FC $M(T)$), which display several features related to strong interactions among MNPs in both samples.

Dynamic measurements (ac susceptibility and SAR) were performed on SPH-E and FAC-E to verify the scaling with $-T\cdot\ln(2\pi f\tau_0)$ predicted by theory. $\chi''(T)$ curves, recorded at the

same H_0 value and several frequencies (Figure 3A,D), present broad peaks. This reflects a wide distribution of E_b values due to size distribution (magnetic volume) and/or the magnetic interactions arising from the MNP arrangement in the samples. Another feature indicative of magnetic interactions is the increasing χ''_{max} values as frequency increases.[13] For the scaling (Figure 3C,F), all magnitudes were normalized dividing by their maximum value, *i.e.*, χ''_{max} or SAR_{max}. The τ_0 values of the scaling variables were obtained from Arrhenius plot of $\chi''(T)$ data (see Figure S3). In the case of SPH-E, the scaling produces very good data collapse of $\chi''(T)$ and SAR(T) curves. Note that SAR(T) was measured with different H_0 and f values (Figure 3B,C). This good collapse is in accordance with the assumption that, even in presence of strong interactions, relaxation times can be described using equation 3 with modified attempt times and/or energy barriers. However, the scaling fails to make $\chi''(T)$ and SAR(T) data collapse for FAC-E. $\chi''(T)$ curves, recorded at the same H_0 value and several frequencies, do collapse, but SAR(T) curves, this time obtained with the same frequency and different H_0 values, do not collapse either among them, or with $\chi''(T)$ curves. The origin of this discrepancy is found in raw SAR(T) data (Figure 3E). The blocking temperature shifts to lower values as H_0 increases. This fact points to an effect of H_0 in relaxation times that is not reflected in the abovementioned theoretical expressions, and has, to the best of the authors' knowledge, never been described theoretically or experimentally. This deviation from LRT occurs even though the H_0 values lie within the limits of the LRT validity. Sample FAC-E is then the first experimental evidence of this deviation.

Self-assembly upon matrix solidification of faceted nanoparticles. In order to shed light on the detected SAR dependence on H_0, another sample prepared with FAC MNPs was selected for study, **FAC-C24**. To prepare it, MNPs were first dispersed in melted n-tetracosane and the liquid was then rapidly solidified inside a small cylindrical container (see SI and scheme II in Figure 2). It has an average concentration of $8.97 \cdot 10^{-3}$ g/g. TEM images of FAC-C24 (Figure 2G-K) reveal a distinct arrangement from that of FAC-E. While in FAC-E big disordered clusters were predominant, in FAC-C24 other structures appear, which seems the result of MNPs segregation to solidification fronts during n-tetracosane solidification. These are chains and elongated two-dimensional arrangements, mainly with hexagonal, but also with square symmetry, typical of cubic MNPs.[33] Due to the lack of homogeneity in shape and size of these MNPs, the orientation inside an arrangement is not constant. This produces more ill-defined spots within the reciprocal space than those in SPH-E ordered areas (Figure 2D). But despite their heterogeneity, FAC MNPs are able to get closely packed and keep similar interparticle distances. Eventually, these closely packed structures are randomly oriented within the sample and appear isolated or surrounding disordered clusters smaller than those in FAC-E.

Due to the container dimensions, *M(H)* measurements of FAC-C24 with the cylinder axis perpendicular to the applied dc field were impossible. Thus, in this case, only $M(H)$ data with the applied dc field parallel to the cylinder axis were obtained. Nevertheless, they reveal that the susceptibility of FAC-C24 at low H is more than the double than that of FAC-E (Figure S2). This result points to a change related either to magnetic interactions and/or to the presence of a preferential alignment of the MNPs. This magnetization increase is also reflected in ZFC/FC *M(T)* curves (Figure S2), which display the same features related to strong interactions than those of FAC-E.

$\chi''(T)$ data at the same H_0 but different f (Figure 3G) present much narrower peaks than those of FAC-E, revealing a more limited distribution of E_b. SAR(T) measurements were performed both parallel and perpendicular to the cylinder axis (Figure 3H). A small difference is found, both in SAR_{max} and in T_b, highlighting a certain global anisotropy in the sample. However, SAR_{max} of FAC-24 in both orientations is more than 16 times that of FAC-E. A potential preferential orientation of chains and two-dimensional arrangements inside FAC-C24 plays thus a minor role when compared to FAC-E. Further confirmation comes from TEM observations, which show random orientation of the aggregates and clusters inside the sample (Figure 2G). Nevertheless, the great differences observed between both samples may lie in the preferential orientation *inside* each arrangement.

It has been shown that spontaneous self-assembly of MNPs during a non-equilibrium process such as solvent evaporation (or, as in FAC-C24, upon segregation at solvent solidification fronts) may lead, under certain conditions, to organization of the particles into structures with long-range order (note that the MNP assembly in Figures 1A and 2I seems alike).[34,35] Dipolar interactions become increasingly important as MNPs get closer, and their anisotropic character leads to collective magnetic ordered structures, including magnetic ordering of the MNPs moments upon assembly formation.[16,35-38] In addition, elongated arrangements of MNPs (predominant in FAC-C24) have been reported to have domain walls along the length of the assembly, with ferromagnetically ordered chains along the length direction. In closed-packed lattices nearest neighbor chains couple FM, and consequently FM ordering is favored locally (in the particular assembly).[40] Moreover, upon magnetic field reversal, domain wall sweep proceeds in the transversal direction of the elongated assembly, *i.e.* keeping the longitudinal alignment.[38] In addition, Monte Carlo simulations of anisotropic clusters have shown that the magnetic moments of chain and cylinders tend to be aligned with the axis of morphology anisotropy[39] and also that the alignment may improve the heating ability of chains and cylinder clusters at most of the angles between the AMF and cluster axis.[40] All these findings support a local preferential orientation in FAC-C24. The SAR/f values (energy dissipated per AMF cycle) of FAC-C24 are comparable (see Figure S4) with high SAR values reported in the literature,[26,41-45] obtained with similar H_0 values. Due to these high SAR values, the arrangements in FAC-C24 are highly interesting for heat dissipation applications, like magnetic hyperthermia.

Figure 3I shows that the $-T \cdot \ln(2\pi f \tau_0)$ scaling fails resoundingly due to a more marked $T_b(H_0)$ dependency. In addition in FAC-C24 (and also in FAC-E), the SAR_{max} data follow a power law $SAR_{max} \propto H_0^m$ with m = 1.9 (see Figure S4), close to the expected dependency for SPM MNPs (equation 1). However, if m is evaluated in FAC-24 at a fix T, a gradual m variation is found, from 3 at 200 K to 1.4 at 300K. This is a direct effect of the $T_b(H_0)$ dependency, which in turn may be another consequence of the acquired MNP arrangements in FAC-C24.

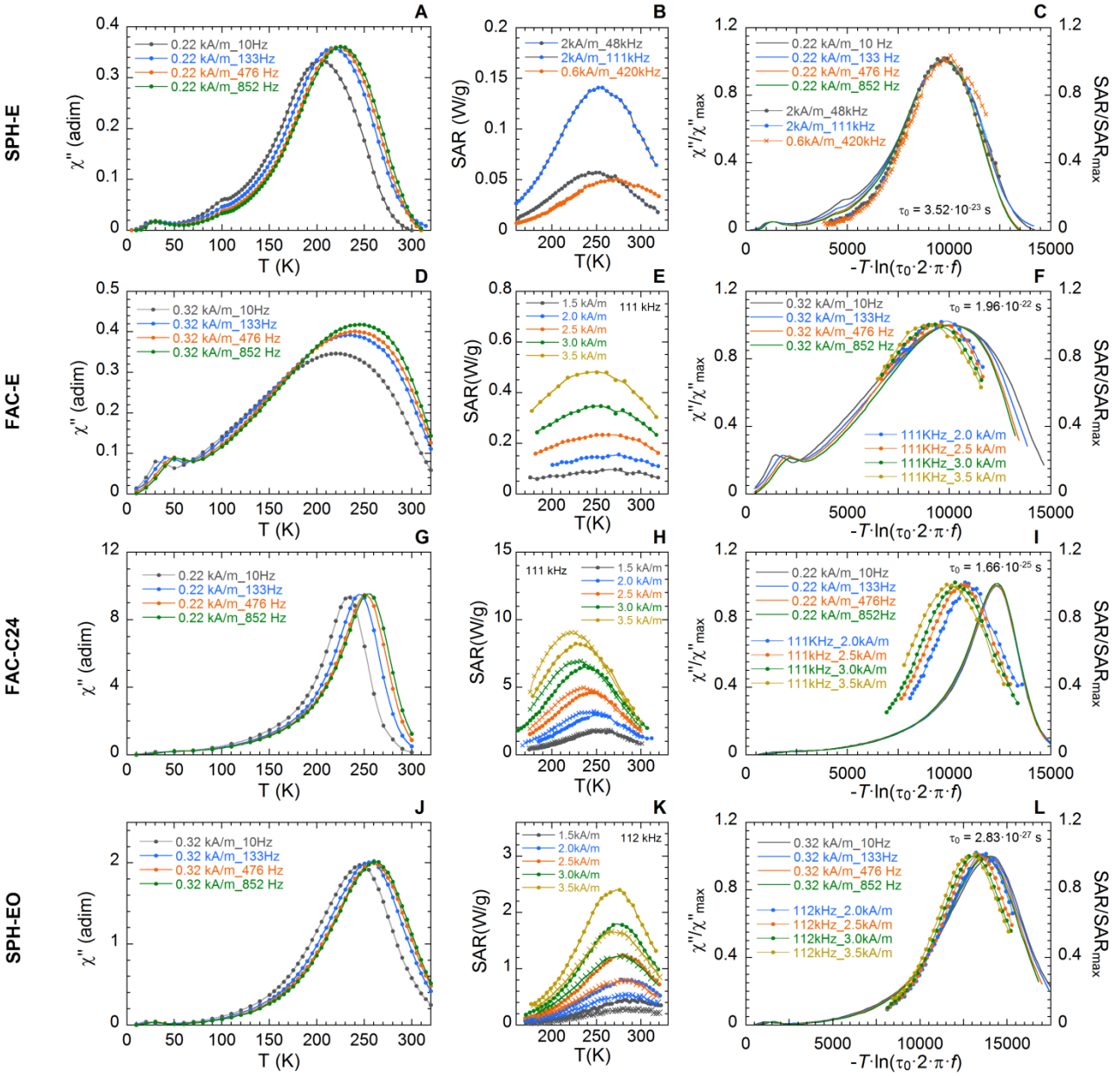

Figure3. For the four MNP assemblies considered (SPH-E, FAC-E, FAC-C24 and SPH-EO), left: out-of-phase component of the ac susceptibility, $\chi''(T)$ at several H_0 and f values, measured with the sample axis parallel to the AMF direction; middle: SAR(T) at several H_0 and f values, recorded with the sample axis parallel (circles) and perpendicular (crosses) to the AMF direction; right: scaling with $-T\cdot\ln(2\pi f\tau_0)$ to verify the collapse among $\chi''(T)$ and SAR(T) curves, using left and middle (just parallel) data and normalizing each curve dividing by its maximum value (χ''_{max} or SAR_{max}). The τ_0 value used for the scaling variable (obtained from Arrhenius plots) is given for each sample. Note that these values are well below the expected values (10^{-27} -·10^{-22} s << 10^{-8} – 10^{-10} s), as it usually occurs in highly interacting systems.

Magnetic field-assisted arrangement of spherical nanoparticles. The fail in the data collapse in samples FAC-E and FAC-C24 could be attributed to the preferential orientation within the aggregates of FAC MNPs upon self-organization. Sample SPH-E, which fulfilled the LRT theory, does not display such preferential orientation. To test the behavior of oriented SPH MNPs, a fourth sample was prepared embedding SPH MNPs into epoxy resin, in presence of a strong static magnetic field parallel to the cylindrical mold axis (see SI and scheme III in Figure 2). This field-oriented sample was named **SPH-EO**. It has an average concentration of $7.69\cdot10^{-3}$ g/g and presents a macroscopic MNP arrangement in form of spikes oriented parallel to the tube axis and visible to the naked eye (Figure S6). TEM images revealed that the cross-section of the macroscopic spike structure is formed by highly-packed ordered areas surrounded by more disperse and disordered zones (Figure 2L-N), in contrast to sample SPH-E, in which ordered areas are rare. Each highly-packed ordered area displays several domains, corresponding to different orientations of the MNP packing. TEM images of sections parallel to the sample

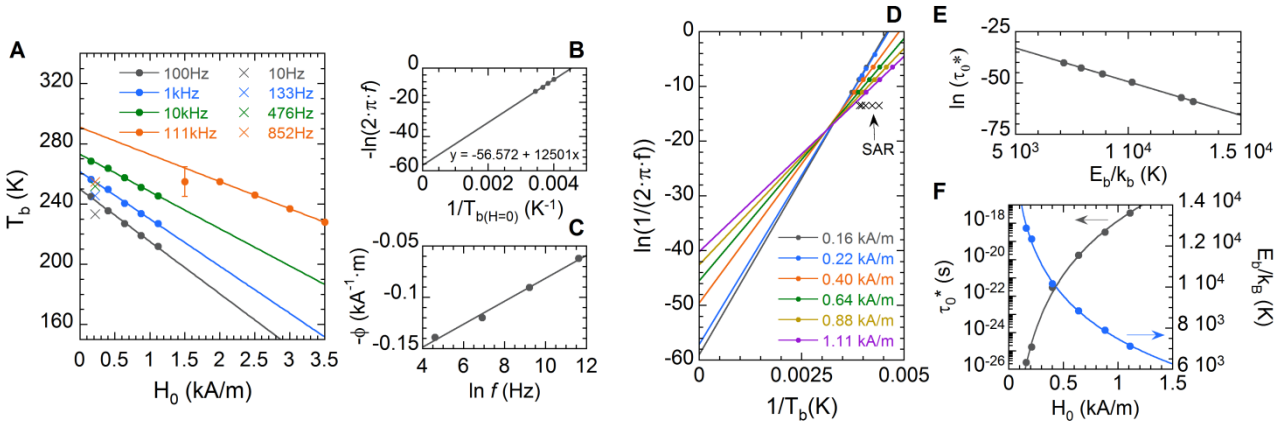

Figure 4. Analysis of $T_b(H_0)$ data for FAC-C24. A: T_b values (circles) extracted from Figure 3H (parallel) and Figure S2 fitted to a linear dependence with H_0, together with T_b values (crosses) extracted from Figure 3G. B: Arrhenius plot of $T_{b(H=0)}$ (see equation 4). C: frequency dependence of $-\phi(f)$ (see equation 4). D: Arrhenius plot of T_b values (circles) extracted from Figure 3G and S2, fitted to one linear trend per H_0 value; T_b values (crosses) extracted from Figure 3H are also plotted. E: relationship between the $\tau_0^*(H_0)$ and $E_b(H_0)$ values (see equation 8) obtained from the linear fitting in D. F: H_0 dependence of $\tau_0^*(H_0)$ and $E_b(H_0)$ in E, fitted to a power and a logarithmic dependence, respectively .

axis were also acquired, revealing similar arrangements (Figure S6).

An overall anisotropy in this sample was detected through $M(H)$ data (Figure S2). While the susceptibility of SPH-EO with the applied dc field perpendicular to the sample axis is similar to that of SPH-E with the dc field in *parallel* direction, that of SPH-EO with the applied dc field parallel to the sample axis is about the double at 100 Oe (8 kA/m). This fact points to a preferential orientation of the MNPs in SPH-EO, as expected due to the field-assisted preparation process. Accordingly, ZFC/FC $M(T)$ curves of SPH-EO display similar features related to strong interactions than the other samples, with higher M values than those of SPH-E, but still lower than those of FAC-C24.

Figure 3K shows SAR(T) data for SPH-EO measured with the ac field both parallel and perpendicular to the sample axis. Similarly to FAC-E and FAC-C24, SPH-EO displays a $T_b(H_0)$ dependence, which supports the conclusion that it is the MNP orientation that gives rise to deviations from the LRT. However, differences are observed between the SAR(T) behavior of FAC-C24 and SPH-EO (Figures 3H and 3K, respectively). In the former, parallel and perpendicular SAR(T) show similar values but different $T_b(H_0)$ values, while in the later, perpendicular SAR(T) data are visibly lower than parallel, although $T_b(H_0)$ values are very similar. These differences between parallel and perpendicular SAR(T) data are most probably due to the fact that MNPs in SPH-EO present an overall orientation along the sample axis, while MNPs in FAC-C24 display *local* orientation within elongated arrangements, but these arrangements do only mildly present a preferred orientation with the sample axis. Also, SAR(T) of FAC-C24 remains higher (more than three times) than that of SPH-EO, which is attributed to the particular arrangement acquired by faceted irregular FAC MNPs. Eventually, Figure 3L shows how the data scaling of $\chi''(T)$ and SAR(T) data fails again due to the $T_b(H_0)$ dependence.

Empirical model for the T_b dependence on H_0 and f at low ac fields. In sum, FAC-E, FAC-C24 and SPH-EO display a T_b dependence on H_0 at low ac fields. We have investigated further sample FAC-C24, with a more marked effect, to explore in greater depth this dependency. For this purpose, additional $\chi''(T)$ data sets at a fix f but with different H_0 (Figure S7) have been recorded. The $T_b(H_0)$ dependency is present at values as low as 2 Oe (0.16 kA/m), well within the LRT validity range for these MNPs. Figure 4A summarizes all T_b values obtained from sample FAC-C24 parallel to the ac field, from Figures 3G, 3H and S7, plotted against H_0. Blocking temperatures determined at the same f exhibit an exceptionally good linear dependence with H_0 that can be described as

$$T_b = T_{b(H=0)} \cdot (1 - \phi(f) \cdot H_0) \qquad (4)$$

where $T_{b(H=0)}$ is the T_b value at zero H_0 ($T_{b(H=0)}$ depends on f), and $-T_{b(H=0)} \cdot \phi(f)$ is the slope of the $T_b(H_0)$ curve at each f. Note that a similar linear dependency can be found also in FAC-E and SPH-EO (see Figure S8). Figure 4B demonstrates that $T_{b(H=0)}$ values do fit well to an Arrhenius dependence, as expected from theory, but with a very low attempt time ($2.70 \cdot 10^{-25}$ s) and a quite high energy barrier ($E_b/k_B = 12501$ K). Note that E_{b0}/k_B for FAC MNPs ranges between 2343 and 4177 K considering only the magnetocrystalline[12] contribution for K_{eff}. $\phi(f)$ shows a decreasing logarithmic dependence with f (Figure 4C).

Based on the above, one could assume as first approach that the observed T_b behavior is a consequence of the ac magnetic field perturbing the energy barrier of the assemblies in absence of field, $E_{b(H=0)}$. According to this,

$$\tau_N = \tau_0 exp\left(\frac{E_{b(H=0)}(1-\phi(f)\cdot H_0)}{k_B T}\right) \qquad (5)$$

with $\phi(f) \cdot H_0 << 1$. Within this assumption, τ_0 is considered independent of H_0, and E_b depends on H_0 and f.

However, Arrhenius plots of $-ln(2\pi f)$ versus $1/T_b$ for $T_b(H_0)$ show that τ_0 actually depends on H_0 (Figure 4D): instead of having a single linear dependence, each H_0 value gives a different slope and intercept in the Arrhenius plot. From this plot, two main results are derived: i) the attempt time depends on H_0; ii) a single E_b value can be obtained for each H_0 at any frequency. Then, a new expression is proposed for τ_N,

$$\tau_N = \tau_0^*(H_0) \cdot exp\left(\frac{E_b(H_0)}{k_B T}\right) \qquad (8 \text{ to } 6)$$

which accounts for the H_0 dependence both in the attempt time and the barrier energy, and eliminates the E_b dependence on f. Figure 4E shows that $\ln \tau_0^*$ and E_b display a linear relationship, which allows τ_0^* to be defined as,

$$\tau_0^*(H_0) = \tau_0 \cdot exp\left(-\frac{E_b(H_0)}{k_B T_{ref}}\right) \qquad (9 \text{ to } 7)$$

where $\tau_0 = 6.47 \cdot 10^{-8}$ s (of the order of expected values of the attempt time of a single MNP) and T_{ref} is an empirical parameter with a value of 305 K for FAC-C24.

Equation 7 is certainly a remarkable result: we have been able to probe different E_b values in sample FAC-C24, and found an unheard-of relationship between τ_0^* and E_b. This sweeping has been possible, due to the particular arrangement of the sample, just changing H_0, without the necessity of modifying any characteristic of the sample (concentration, arrangement…) or of applying dc magnetic fields.

It is experimentally observed that τ_0^* shows a power dependence on H_0 (Figure 5F) that can be expressed as,

$$\tau_0^*(H_0) = \tau_0 \cdot \left(\frac{H_0}{H_{ref}}\right)^n \qquad (10 \text{ to } 8)$$

where n = 9.9 and H_{ref} = 12.01 kA/m (n and H_{ref} are also empirical parameters). τ_0^* is initially very small and gets longer with increasing H_0. Combining equations 7 and 8,

$$E_b(H_0) = -n \cdot T_{ref} \cdot k_B \cdot ln\left(\frac{H_0}{H_{ref}}\right) \qquad (11 \text{ to } 9)$$

According to equation 9, $E_b(H_0)$ follows a decreasing logarithmic trend with H_0 (in agreement with Figure 4C). As a consequence, τ_N (equation 7) decreases as H_0 increases. At T_b,

$$T_b(H_0, f) = T_{ref} \cdot \frac{n \cdot ln\left(\frac{H_0}{H_{ref}}\right)}{n \cdot ln\left(\frac{H_0}{H_{ref}}\right) + ln(2\pi f \tau_0)} \qquad (12 \text{ to } 10)$$

expression that approximately yields a linear dependence with H_0 for the experimental range in the present work.

Modeling $\chi''(T)$ and SAR(T) using T_b and the size distribution. It has been widely demonstrated[13,46] that analyzing the whole $\chi''(T)$ and/or SAR(T) curves of a MNP system allows to extract more information than just studying T_b data. However, the interpretation of these curves is not straightforward, since they are often a convolution of several $\chi''(T)$ and/or SAR(T) curves due to an E_b distribution,. The comparison between Figures 3D and 3G or between Figures 3E and 3H (same FAC MNPs, different arrangement) reflects the above. T_b values for FAC-E and FAC-C24 are slightly different, but the main striking difference between the samples are the shape and absolute values of their $\chi''(T)$ and SAR(T) curves. Thus, continuing with the focus on sample FAC-C24, we modeled $\chi''(T)$ and SAR(T) data including the effect of size distribution. At first sight, these data display a main sharp peak at high T and a tail towards low T that suggests a convolution of several E_b distributions. But given that T_b has been estimated from the main peak, the modeling was restricted to reproduce the data for the temperatures near and above T_b.

The modeling was made using the E_b distribution related to the MNP size derived by TEM and also the previously obtained results from the empirical model of T_b, in particular $T_b(H_0,f)$, $\tau_0^*(H_0)$ and $E_b(H_0)$ values. Given that for SAR(T) no experimental $\tau_0^*(H_0)$ and $E_b(H_0)$ data could be obtained (*i.e.*, at H_0 and f values of SAR measurements), the modeling of SAR(T) data was made using: i) $\tau_0^*(H_0)$ data calculated according to equation 8; ii) $E_b(H_0)$ data using equation 6 at $T = T_b$. A detailed description and an example of this modeling are given in the SI (section 10 and Figure S9). The first conclusion derived while trying to model the $\chi''(T)$ and SAR(T) curves including the size distribution is that E_b cannot be defined just as $K_{app} \cdot V$, (even increasing the magnitude of K_{app} assuming that it contains interaction effects) since the obtained $\chi''(T)$ and SAR(T) curves are wider than the experimental data. Due to this, E_b was redefined as,

$$E_b = E_{arr} + K_{app} \cdot V \qquad (13 \text{ to } 11)$$

where E_{arr} stands for a contribution to the energy barrier of the dipolar interactions established by the specific MNP arrangement in FAC-C24. Figure 5 collects the values of the E_{arr} and K_{app} parameters derived from the modeling. E_{arr} decreases with H_0, with an identical logarithmic trend for all f values. The trend of K_{app} is more unclear. It seems to slightly decrease with H_0 and also to present some dependency on f. But the values at 111 kHz, which show the highest decrease, are those obtained with calculated $\tau_0^*(H_0)$ values, and therefore the most uncertain. The rest of K_{app} values range between 13-17 kJ/m^3, below the magnetocrystalline anisotropy constant of bulk Fe_3O_4, but in accordance with experimental results obtained for MNPs.[47]

At this point, two different definitions of E_b have been given, namely equations 9 and 11: the former obtained from the analysis of T_b, and the later, from the modeling of $\chi''(T)$ and SAR(T). However, they are compatible descriptions. As shown in Figure 5A, E_{arr} data can be fitted with the function described by equation 9. Fixing n = 9.9 and T_{ref} = 305 K (fitting parameters of E_b in Figure 4F), an acceptable fit is obtained with H_{ref} = 6.26 kA/m. Then, we can approximate,

$$E_{arr}(H_0) \cong -n \cdot T_{ref} \cdot k_B \cdot ln\left(\frac{H_0}{H_{ref}^*}\right) \qquad (14 \text{ to } 12)$$

with a new empirical parameter, H_{ref}^* = 6.26 kA/m. Combining equations 9, 11 at T_b, (*i.e.* $E_b = E_{arr} + K_{app} \cdot V_{max}$) and 12,

$$E_b - E_{arr} = K_{app} \cdot V_{max} \cong n \cdot T_{ref} \cdot k_B \cdot ln\left(\frac{H_{ref}}{H_{ref}^*}\right) \qquad (15 \text{ to } 13)$$

where V_{max} is the MNP volume whose T_b is that of the maximum of $\chi''(T)$ or SAR(T). As obtained from the modeling (see Table S3) V_{max} is $1.95 \cdot 10^{-24}$ m^3, so K_{app} = 13.92 kJ/m^3. This value is comparable to the results in Figure 5B. This analysis allows correlating equations 11 and 13 if the uncertain dependence of K_{app} on H_0 and f are neglected (hence the approximation symbol in equations 12 and 13). The energy barrier of FAC-C24 is then successfully described with a typical anisotropy term ($K_{app} \cdot V$) and an additional contribution due to the sample arrangement (E_{arr}) that decreases logarithmically as H_0 increases. According to this, equation 7 can be rewritten as,

$$\tau_0^*(H_0) \cong \tau_0 \cdot exp\left(-\frac{E_{arr}(H_0)}{k_B T_{ref}}\right) \qquad (16 \text{ to } 14)$$

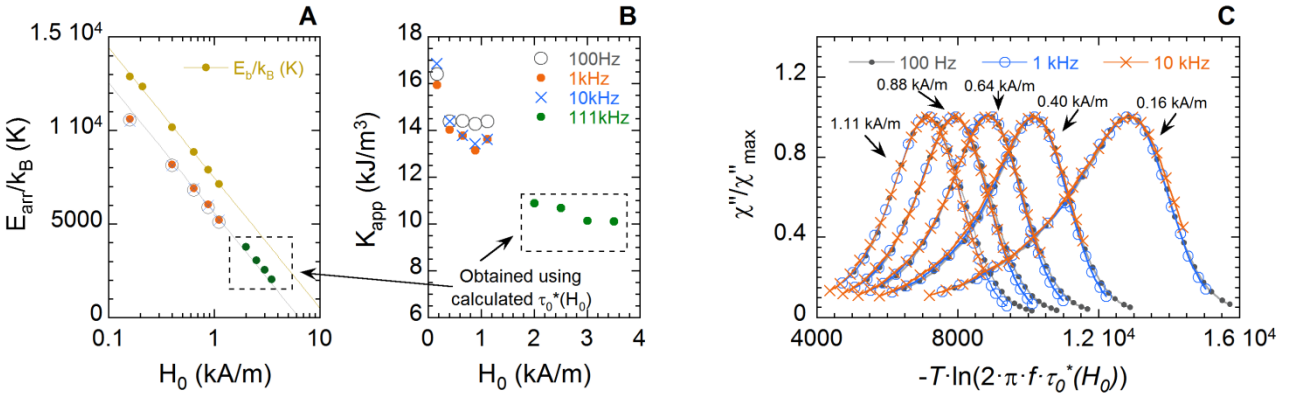

Figure 5. Field amplitude dependency of E_{arr}/k_B (A) and K_{app} (B) obtained for FAC-C24 from the modeling of data in Figure 3H (parallel) and Figure S2, according to equation 13. E_{arr}/k_B data are fitted to equation 11, and are plotted together with E_b/k_B values (Figure 5) fitted to the same equation. C: collapse of $\chi''(T)$ data in Figure S2 (FAC-C24) using $-T\cdot\ln(2\pi f\tau_0^*(H_0))$ as scaling variable and the $\tau_0^*(H_0)$ values in Figure 5F.

where $\tau_0 = 1.02\cdot10^{-10}$ s (in the order of magnitude of expected values). Accordingly τ_N (equation 6) turns into,

$$\tau_N = \tau_0 \cdot exp\left(-\frac{E_{arr}(H_0)}{k_B T_{ref}}\right) \cdot exp\left(\frac{E_{arr}(H_0)+K_{app}\cdot V}{k_B T}\right) \quad (17 \text{ to } 15)$$

which is the final output of our empirical model. Within this approximation, it can be concluded that the experimental observation of the variation of T_b with H_0 is indicative of the existence of E_{arr} and thus a sign of particular magnetic interactions related to MNP preferential orientation. Moreover, Figure 5C shows the data collapse of $\chi''(T)$ data from Figure S7 using $-T\cdot\ln(2\pi f\tau_0^*(H_0))$ as scaling variable and the $\tau_0^*(H_0)$ values in Figure 4F. The curves recorded with the same frequency show a very good collapse, which supports the τ_N dependency proposed in equations 6 and 15. Accordingly, Figure 5C reflects that $E_b(H_0)$ is independent of f and gets shifted to lower energies as H_0 increases. In conclusion, equations 6 to 15 succeed in describing the behaviour of FAC-C24.

The same modeling was performed for the sample with opposite behavior, SPH-E. Note that, given that all $\chi''(T)$ and SAR(T) data show a good collapse (Figure 3C), the parameters resulting from the modeling are common for all curves. Using the E_b/k_B (9714 K) and τ_0^* ($3.62\cdot10^{-23}$ s) values derived from the Arrhenius plot, as well as the TEM size distribution, an excellent reproduction of the curves (Figure S10) was obtained with E_{arr} = 0 and K_{app} = 56.99 kJ/m^3. Contrarily to FAC-C24, this sample does not display an additional contribution to the energy barrier due to the arrangement. However, dipolar interactions are most probably affecting its K_{app} value. Modeling of FAC-E was also attempted, but it failed because of the complex convolution presented by the main peaks, most probably due to sample arrangement heterogeneity.

Lastly, modeling of $\chi''(T)$ data of SPH-EO using the τ_0^* ($2.83\cdot10^{-27}$ s) and E_b/k_B (13873 K) values obtained from the Arrhenius plot (Figure S3) gives good reproduction of the curves (Figure S10) with E_{arr}/k_B = 3676 K and K_{app} = 59.83 kJ/m^3. The MNP orientation provides SPH-EO with a $E_{arr} \neq 0$, as opposed to SPH-E. This finding supports the existence of a contribution to the energy barrier (independent from MNP volume distribution) established by anisotropic MNP arrangements with local orientation of MNPs. Note, however, that the E_{arr} of FAC-C24 is more than double for the same H_0. This difference is in accordance with other differences (arrangement, magnetic and magnetothermal properties) between samples FAC-C24 and SPH-EO.

Physical interpretation of the empirical model parameters. The empirical model described above is supported on several empirical parameters, namely T_{ref}, H_{ref}^*, n and E_{arr} (H_{ref} is determined by the other parameters and $K_{app}\cdot V_{max}$, see equation 13). In order to find a physical interpretation for these parameters, we have explored different analytical models that include dipolar magnetic interactions.[13,48-51] Among them, we have focused on the Dormann-Bessais-Fiorani[51] (DBF) model that is in best accordance with equation 15 in the sense that it reflects a dependency of τ_0^* on E_b. The DBF model provides analytical expressions for the τ_N of an arrangement of non-identical (*i.e.*, with a certain volume distribution) MNPs with dipolar interactions of different strength.

For the case of strong dipolar interactions, this model derives an expression for a modified E_b, valid if $\beta = (\mu_0/4\pi)\cdot(M_S^2\cdot\bar{\boldsymbol{V}}\cdot a_1/k_BT) \geq 2$. Considering only interactions with first neighbors, SI units, and rearranging E_b (see SI section 7, for details) τ_N can be expressed as,

$$\tau_N = \tau_0 \cdot exp(-E_d/E_{di}) \cdot exp\left(\frac{K_{eff}\cdot V + E_d}{k_B T}\right) \quad (18 \text{ to } 16)$$

where,

$$E_d = \frac{\mu_0}{4\pi}\cdot M_S^2 \bar{V} n_1 b_1 \quad \text{and} \quad E_{di} = \frac{\mu_0}{4\pi}\cdot M_S^2 \bar{V} a_1 \quad (19 \text{ to } 17)$$

$\bar{V}$ is the mean particle volume, n_1 is the number of MNPs that are first neighbors of a given MNP, $a_1 = \bar{V}\cdot(3\cdot\cos^2\alpha_1 - 1)/d_1^3$, α_1 is a mean angular parameter related to the MNP arrangement, d_1 is the distance between the center of a given MNP and those of its first neighbors, and b_1 is a parameter similar to a_1 that accounts for slight differences between MNPs (V and d_1). Equation 16 is qualitatively in accordance with the described empirical model provided that $E_d \equiv E_{arr}$ and $E_{di} \equiv k_B\cdot T_{ref}$. Therefore, $E_d/E_{di} = E_{arr}/(k_B\cdot T_{ref}) = n_1\cdot b_1/a_1$. This indicates that both E_{arr} and $k_B\cdot T_{ref}$ are correctly related to dipolar interaction energies related to the MNP arrangement of closely packed MNPs.

As stated above, equation 16 is valid if $\beta \geq 2$. To estimate the maximum β values possible for FAC and SPH MNPs, the maximum a_1 must be calculated. From TEM images of samples

FAC-C24 and SPH-EO, where MNPs are closely packed, d_1 has been roughly estimated as 16.5 nm and 18 nm, respectively. In the extreme case $\cos^2\alpha_1 = 1$, the maximum a_1 and β values at 250 K are, respectively, 0.62 and 4.5 for FAC MNPs, and 0.79 and 5.75 for SPH MNPs. Then these MNPs can fulfill equation 16 provided that $\cos^2\alpha_1$ is high enough. In more detail, α_1 is a parameter that represents, in average, the angle between the line joining two MNP centers (a reference MNP and a first neighbor) and the direction of the magnetic moment of the first neighbor. Then, $\cos^2\alpha_1$ is maximal in the case of a chain of MNPs whose magnetic moments are oriented in the chain axis direction, is lower in the case of other oriented MNP arrangements, and even lower in the case of MNP arrangements of random orientation.

However, if β is calculated from the empirical values obtained for FAC-C24, then $\beta = T_{ref}/T = 1.22 < 2$ at 250 K. Also, from the Arrhenius plot of SPH-EO (Figure S3) assuming $\tau_0 = 10^{-10}$ s in equation 14, $T_{ref} = 96$ K and $\beta = T_{ref}/T = 0.39 << 2$ for 250 K. Then, a discrepancy arises, since both FAC-C24 and SPH-EO have been experimentally found to have established an E_{arr}, but their β values are not high enough to create E_{arr} according to the DBF model. This apparent conflict can be explained as the DBF model is based on a unique MNP regular arrangement, but the arrangement of FAC-C24 and SPH-EO is irregular, presenting diverse MNP ordering and even randomly ordered areas (SPH-EO). Then, the average a_1 is probably lower than certain a_1 values of ordered areas that fulfill $\beta \geq 2$ locally. In addition, estimation of the DBF factor $n_1 \cdot b_1/a_1$ from the empirical values derives values of 29.4 and 38.3 for FAC-C24 and SPH-EO, respectively, at $H_0 = 0.32$ kA/m. 2D arrangements are predominant in FAC-C24, so that $n_1 \cong 6$, and thus $b_1/a_1 \cong 4.9$. For the 3D arrangements in SPH-EO one can assume $n_1 \cong 12$, and $b_1/a_1 \cong 3.2$. These values seem quite high, considering that b_1 accounts for slight differences in V/d_1^3 between MNPs.

Eventually, the DBF model does not predict any explicit dependency of E_{arr} with H_0. However, according to equation 16 and our analysis, the only parameter that could be subject to variation with H_0 is n_1 ($n_1 \cdot (b_1/a_1) = E_{arr}/(k_B \cdot T_{ref}) \cong -n \cdot \ln(H_0/H_{ref}^*)$). This dependency could be explained on the basis of the preferential alignment of the MNP easy axes in the arrangement. At zero temperature, one may picture the magnetic moments preferentially aligned, leading to a strong anisotropic interaction. As temperature increases, some of the MNPs become close to their T_b. The H_0 field component along the preferential orientation helps the MNPs to overcome E_b and become SPM, with their magnetic moments not in a fixed direction anymore. As H_0 increases, the population of MNPs that stays on the blocked state (contributing to E_{arr}) decreases, thereby reducing the effective n_1 value and the strength of dipolar interactions. Within this picture, larger H_0 would promote MNPs to become SPM at lower blocking temperatures, as our results indicate. Then the DBF model is consistent also with $E_{arr}(H_0)$. In accordance with empirical parameters n and H_{ref}^*, the population of MNPs quitting a preferred orientation in the arrangement shows a potential dependence with H_0, and the preferred orientation should disappear at H_{ref}^*.

For the sake of comparison, the observed effect of H_0 on E_{arr} would be equivalent to the application of a static magnetic field, H_{dc}, to a non-interacting system. For example, the Stoner-Wohlfarth model[52] provides an expression very similar to that of E_b in equation 5 (see SI for further discussion and more experimental data about this equivalence), although this model does not comprise thermally-induced relaxations. Similar results are obtained by Monte Carlo simulations.[53] In absence of interactions (*i.e.* in absence of E_{arr}) and in randomly oriented MNPs, it is shown that increasing H_{dc} progressively reduces E_b and narrows the width of the peaks. Consequently, the scaling variable for data collapse also depends on H_0. In our samples, H_0 reduces the additional term to E_b (E_{arr}) created by interactions.

In conclusion, a novel effect has been discovered by combining magnetic susceptibility measurements and SAR(T) characterization over carefully selected arrangements of superparamagnetic spherical and faceted magnetite nanoparticles: in closely-packed ordered anisotropic assemblies, Néel relaxation time (τ_N) depends on the amplitude of the applied alternating magnetic field (H_0) at sufficiently low H_0 values to lie within the linear response theory range. As a consequence, the blocking temperature (T_b) varies linearly with H_0 and there is one Ahrrenius plot for each H_0 value. In addition, the scaling variable - $T \cdot \ln(2\pi f \tau_0)$ fails in making collapse $\chi''(T)$ and SAR(T) data for different frequencies. Also, SAR does not increase as H_0^2, but follows a power law whose exponent changes with temperature. Both the attempt time (τ_0^*) and the barrier energy (E_b) depend on H_0 through E_{arr}, a strong interaction energy contribution created by the ordered anisotropic assemblies. In turn, $E_b = E_{arr} + K_{app} \cdot V$, *i.e.*, E_{arr} does not depend on the particle volume, thus not contributing to the increase in K_{app}. Then E_{arr} does not originate a widening of the E_b distribution, avoiding a highly detrimental effect of magnetic interactions that strongly decrease absolute SAR values. The decrease of E_{arr} with H_0 is related to an increase in the number of nanoparticles whose magnetic moment is leaving (near T_b) the preferred orientation induced by the anisotropic arrangement morphology. All these effects are stronger in faceted nanoparticles that have self-assembled in relatively small anisotropic arrangements upon matrix solidification, than in spherical particles that have been ordered in visible spikes under a static magnetic field. Accordingly, the origin of E_{arr} is assigned to the local preferential orientation of nanoparticles inside anisotropic assemblies. In sum, this work highlights the essential role of arrangement in obtaining high SAR values at low H_0, and provides a further step towards the understanding and prediction of the magnetic properties and heating ability of closely-packed self-assemblies of superparamagnetic nanoparticles displaying collective effects.

ASSOCIATED CONTENT

Supporting Information

Rosensweig's model of superparamagnetism and linear response theory; magnetic nanoparticles and preparation of MNPs assemblies; experimental techniques; $M(H)$ and ZFC/FC $M(H)$ curves; Arrhenius plots; some considerations about SAR values; spikes in SPH-EO; $\chi''(T)$ data of sample FAC-C24 at a fix f but different H_0; variation of T_b with H_0 for samples FAC-E and SPH-EO; modeling $\chi''(T)$ and SAR(T) using T_b and size distribution; DBF model: arrangement of non-identical MNPs with strong dipolar interactions; Stoner-Wohlfarth model with applied H_{dc} and $\chi''(T)$ data of sample FAC-C24 with different superimposed H_{dc} values.

The Supporting Information is available free of charge on the ACS Publications website.

AUTHOR INFORMATION

Corresponding Author

* Email: evanat@unizar.es.

Author Contributions

The manuscript was written through contributions of all authors.

ACKNOWLEDGMENT

This work has been funded by the Spanish MINECO and FEDER, through the projects MAT2014-53961-R and MAT2017-86826-R, by the Aragón government (DGA, group PLATON E31_17R) and by the Centro Universitario de la Defensa de Zaragoza (project no. 2018-06). I.A. thanks the Spanish CSIC for her JAE-Predoc contract. The use of Servicio General de Apoyo a la Investigación-SAI, Universidad de Zaragoza, is also acknowledged.

REFERENCES

1. Reddy, R. L.; Arias, J. L.; Nicolas, J.; Couvreur, P. Nanoparticles: Design and Characterization, Toxicity and Biocompatibility, Pharmaceutical and Biomedical Applications. *Chem. Rev.* **2012**, *112*, 5818-5878.
2. Laurent, S.; Dutz, S.; Häfeli, U.O.; Mahmoudi, M. Magnetic Fluid Hyperthermia: Focus on Superparamagnetic Iron Oxide Nanoparticles, *Adv. Colloid Interface Sci.* **2011,** *166,* 8–23.
3. Mura, S.; Nicolas, J.; Couvreur P. Stimuli-responsive nanocarriers for drug delivery. *Nat. Mater.* **2013**, *12*, 991–1003.
4. Chudzik, B.; Miaskowski, A.; Surowiec, Z.; Czernel, G.; Duluk, T.; Marczuk, A.; Gagos, M. Effectiveness of Magnetic Fluid Hyperthermia Against *Candida albicans* Cells. *Int. J. Hypertherm.* **2016**, *32*, 842-857.
5. Loynachan, C. N.; Romero, G.; Christiansen, M. G.; Chen, R.; Ellison, R.; O'Malley, T. T.; Froriep, U. P.; Walsh, D. M.; Anikeeva, P. Targeted Magnetic Nanoparticles for Remote Magnetothermal Disruption of Amyloid-β Aggregates. *Adv. Health. Mat.* **2015,** *4*, 2100-2109.
6. Puig, J.; Hoppe, C. E.; Fasce, L. A.; Pérez, C. J.; Piñeiro-Redondo, Y.; Bañobre-López, M.; López-Quintela, M. A.; Rivas, J.; Williams, R. J. J. Superparamagnetic Nanocomposites Based on the Dispersion of Oleic Acid-Stabilized Magnetite Nanoparticles in a Diglycidylether of Bisphenol A-Based Epoxy Matrix: Magnetic Hyperthermia and Shape Memory. *J. Phys. Chem. C* **2012**, *116* (24), 13421–13428.
7. Meffre, A.; Mehdaoui, B.; Connord, V.; Carrey, J.; Fazzini, P. F.; Lachaize, S.; Respaud, M.; Chaudret, B. Complex Nano-objects Displaying Both Magnetic and Catalytic Properties: A Proof of Concept for Magnetically Induced Heterogeneous Catalysis. *Nano Lett.* **2015**, *15*, 3241-3248.
8. Ling, D.; Hyeon, T. Chemical Design of Biocompatible Iron Oxide Nanoparticles for Medical Applications. *Small*, **2013**, *9*, 1450-1466.
9. Kozissnik, B.; Bohorquez, A. C.; Dobson, J.; Rinaldi, C. Magnetic Fluid Hyperthermia: Advances, Challenges and Opportunity. *Int. J. Hypertherm.* **2013**, *29*, 76-714.
10. Thiesen, B.; Jordan, A. Clinical Applications of Magnetic Nanoparticles for Hyperthermia. *Int. J. Hyperther.* **2008**, *24*, 467–474.
11. Carrey, J.; Mehdaoui, B.; Respaud, M. Simple Models for Dynamic Hysteresis Loop Calculations of Magnetic Single-Domain Nanoparticles: Application to Magnetic Hyperthermia Optimization. *J. Appl. Phys.* **2011**, *109*, 083921.
12. Rosensweig, R. E. Heating Magnetic Fluid with Alternating Magnetic Field. *J. Magn. Magn. Mater.* **2002**, *252*, 370–374.
13. Landi, G. T.; Arantes, F. R.; Cornejo, D.R.; Bakuzis, A.F.; Andreu, I.; Natividad, E. AC Susceptibility as a Tool to Probe the Dipolar Interaction in Magnetic Nanoparticles. *J. Magn. Magn. Mater.* **2017**, *421*, 138-151.
14. Luis, F.; Torres, J. M.; García, L. M.; Bartolomé, J.; Stankiewicz, J.; Petroff, F.; Fettar, F.; Maurice, J.-L.; Vaurès, A. Enhancement of the Magnetic Anisotropy of Nanometer-Sized Co Clusters: Influence of the Surface and of Interparticle Interactions. *Phys. Rev. B* **2002**, *65* (9), 094409.
15. Urtizberea, A.; Arizaga, A.; Silva, N. J. O.; Millán, A.; Palacio, F.; Luis, F. Texture-Induced Magnetic Interactions in Ferrofluids. *J. Appl. Phys.* **2012**, *111* (9), 093910.
16. Varón, M.; Beleggia, M.; Kasama, T.; Harrison, R. J.; Dunin-Borkowski, R. E.; Puntes, V. F.; Frandsen, C. Dipolar Magnetism in Ordered and Disordered Low-Dimensional Nanoparticle Assemblies. *Sci. Rep.* **2013**, *3*, 1234.
17. Wetterskog, E.; Jonasson, C.; Smilgies, D.-M.; Schaller, V.; Johansson, C.; Svedlindh, P. Colossal Anisotropy of the Dynamic Magnetic Susceptibility in Low-Dimensional Nanocube Assemblies. *ACS Nano* **2018**, *12*, 1403–1412.
18. Wei, A.; Kasama, T.; Dunin-Borkowski, R. E. Self-Assembly and Flux Closure Studies of Magnetic Nanoparticle Rings. *J. Mater. Chem.* **2011**, *21*, 16686–16693.
19. Martinez-Boubeta, C.; Simeonidis, K.; Makridis, A.; Angelakeris, M.; Iglesias, O.; Guardia, P.; Cabot, A.; Yedra, L.; Estrade, S.; Peiro, F.; Saghi, Z.; Midgley, P.A.; Conde-Leboran, I.; Serantes, D.; Baldomir, D. Learning from Nature to Improve the Heat Generation of Iron-Oxide Nanoparticles for Magnetic Hyperthermia Applications, *Scientific Reports* **2013***, 3,* 1652.
20. Andreu. I.; Natividad, E.; Solozabal, L.; Roubeau, O. Nano-objects for Addressing the Control of Nanoparticle Arrangement and Performance in Magnetic Hyperthermia. *ACS Nano* **2015**, *9*, 1408-1419.
21. Orue, I.; Marcano, L.; Bender, P.; García-Prieto, A.; Valencia, S.; Mawass, M.A.; Gil-Cartón, D.; Alba Venero, D.; Honecker, D.; García-Arribas, A.; Fernández Barquín, L.; Muela, A.; Fdez-Gubieda, M.L. Configuration of the magnetosome chain: a natural magnetic nanoarchitecture. *Nanoscale* **2018**, *10*, 7407–7419.
22. Dormann, J.L.; Fiorani, D.; Cherkaoui, R.; Tronc, E.; Lucari, F.; D'Orazio, F.; Spinu, L.; Noguès, M.; Kachkachi, H.; Jolivet, J.P. *J. Magn. Magn. Mater.* **1999**, 203, 23–27.
23. De Toro, J.A.; Normile, P.S.; Lee, S.S.; Salazar, D.; Cheong, J.L.; Muñiz, P.; Riveiro, J.M.; Hillenkamp, M.; Tournus, F.; Tamion, A.; Nordblad, P. Controlled Close-Packing of Ferrimagnetic Nanoparticles: An Assessment of the Role of Interparticle Superexchange versus Dipolar Interactions. *J. Phys. Chem. C* **2013,** *117*, 10213-10219.
24. Anand, M.; Carrey, J.; Banerjee, V. Spin morphologies and heat dissipation in spherical assemblies of magnetic nanoparticles. *Phys. Rev. B* **2016**, *94*, 094425.
25. Natividad, E.; Castro, M.; Mediano, A. Adiabatic Magnetothermia Makes Possible the Study of the Temperature Dependence of the Heat Dissipated by Magnetic Nanoparticles under Alternating Magnetic Fields. *Appl. Phys. Lett.* **2011**, *98*, 243119.
26. Natividad, E.; Castro, M.; Mediano, A. Accurate Measurement of the Specific Absorption Rate Using a Suitable Adiabatic Magnetothermal Setup. *Appl. Phys. Lett.* **2008**, *92* (9), 093116.

27. Labarta, A.; Iglesias, O.; Balcells, L.; Badia, F. Magnetic relaxation in small-particle systems: Ln(t/τ_0) scaling. *Physical Review B* **1993**, *48*, 10240–10246.
28. Berkov, D. V.; Gorn, N. L. Susceptibility of the disordered system of fine magnetic particles: a Langevin-dynamics study *J. Phys.: Condens. Matter* **2001**, *13*, 9369.
29. Mehdaoui, B. ; Tan, R.P. ; Meffre, A. ; Carrey, J. ; Lachaize, S. ; Chaudret, B.; Respaud, M. Increase of magnetic hyperthermia efficiency due to dipolar interactions in low-anisotropy magnetic nanoparticles: Theoretical and experimental results. *Phys. Rev. B*, **2013**, *87*, 174419.
30. Moya, C.; Iglesias, Ó.; Batlle, X.; Labarta, A. Quantification of Dipolar Interactions in Fe3-XO4 Nanoparticles. *J. Phys. Chem. C* **2015**, *119* (42), 24142–24148.
31. Andreu, I.; Natividad, E.; Solozábal, L.; Roubeau, O. Same Magnetic Nanoparticles, Different Heating Behavior: Influence of the Arrangement and Dispersive Medium. *J. Magn. Magn. Mater.* **2015,** *380*, 341-346.
32. Luigjes, B.; Woudenberg, S. M. C.; de Groot, R.; Meeldijk, J. D.; Torres Galvis, H. M.; de Jong, K. P.; Philipse, A. P.; Erné, B. H. Diverging Geometric and Magnetic Size Distributions of Iron Oxide Nanocrystals. *J. Phys. Chem. C* **2011**, *115*, 14598–14605.
33. Yamamuro, s.; Sumiyama, K. Why do cubic nanoparticles favor a square array? Mechanism of shape-dependent arrangement in nanocube self-assemblies. *Chem. Phys. Lett.* **2016**, *418,* 166–169.
34. Rabani, E.; Reichman, D.R.; Geissler, P.L.; Brus, L.E. Drying-mediated self-assembly of nanoparticles. *Nature* **2003**, *426*, 271–274.
35. Ku, J.; Aruguete, D.M.; Alivisatos, A.P.; Geissler, P.L. Self-Assembly of Magnetic Nanoparticles in Evaporating Solution. *J. Am. Chem. Soc.* 2011, **133**, 838–848.
36. Keng, P.Y.; Shim, I.; Korth, B.D.; Douglas, J.F.; Pyun, J. Synthesis and Self-Assembly of Polymer-Coated Ferromagnetic Nanoparticles. *ACS Nano*, **2007**, *1*, 279–292.
37. Varón, M.; Peña, L.; Balcells, L.; Skumryev, V.; Martinez, B.; Puntes, V. Thermoresponsive Vesicular Morphologies Obtained by Self-Assemblies of Hybrid Oligosaccharide-block-poly(N-isopropylacrylamide) Copolymer Systems. *Langmuir* **2010**, *26*, 109–116.
38. Varón, M.; Beleggia, M.; Jordanovic, J.; Schiøtz, J.; Kasama, T.; Puntes, V.F.; Frandsen, C. Longitudinal Domain Wall Formation in Elongated Assemblies of Ferromagnetic Nanoparticles. *Sci. Rep.* **2015**, *5*, 14536.
39. Anand, M.; Banerjee, V.; Carrey, J. Relaxation in One-Dimensional Chains of Interacting Magnetic Nanoparticles: Analytical Formula and Kinetic Monte Carlo Simulations. *Phys. Rev. B* **2019**, *99*, 024402.
40. Fu, R.; Yan, Y.Y.; Roberts, C. Study of the Effect of Dipole Interactions on Hyperthermia Heating the Cluster Composed of Superparamagnetic Nanoparticles. *AIP Adv.* **2015**, 5, 12, 127232.
41. Hergt, R.; Hiergeist, R.; Zeisberger, M.; Schüler, D.; Heyen, U.; Hilger, I.; Kaiser, W. A. Magnetic Properties of Bacterial Magnetosomes as Potential Diagnostic and Therapeutic Tools. *J. Magn. Magn. Mater.* **2005**, *293* (1), 80–86.
42. Józefczak, A.; Hornowski, T.; Skumiel, A.; Łabowski, M.; Timko, M.; Kopčanský, P.; Koneracká, M.; Szlaferek, A.; Kowalski, W. Effect of Poly (Ethylene Glycol) Coating on the Magnetic and Thermal Properties of Biocompatible Magnetic Liquids. *J. Magn. Magn. Mater.* **2009**, *321* (10), 1505–1508.
43. Guardia, P.; Di Corato, R.; Lartigue, L.; Wilhelm, C.; Espinosa, A.; Garcia-Hernandez, M.; Gazeau, F.; Manna, L.; Pellegrino, T. Water-Soluble Iron Oxide Nanocubes with High Values of Specific Absorption Rate for Cancer Cell Hyperthermia Treatment. *ACS Nano* **2012**, *6* (4), 3080–3091.
44. Bender, P.; Fock, J.; Frandsen, C.; Hansen, M. F.; Balceris, C.; Ludwig, F.; Posth, O.; Wetterskog, E.; Bogart, L. K.; Southern, P.; et al. Relating Magnetic Properties and High Hyperthermia Performance of Iron Oxide Nanoflowers. *J. Phys. Chem. C* **2018**, *122* (5), 3068–3077.
45. Kekalo, K.; Baker, I.; Meyers, R.; Shyong, J. Magnetic Nanoparticles with High Specific Absorption Rate at Low Alternating Magnetic Field. *Nano Life* **2015**, *5* (2), 1550002.
46. Jonsson, T.; Mattsson, J.; Nordblad, P.; Svedlindh, P. Energy Barrier Distribution of a Noninteracting Nano-Sized Magnetic Particle System. *J. Magn. Magn. Mater.* **1997**, *168* (3), 269–277.
47. Yoon, S. Determination of the Temperature Dependence of the Magnetic Anisotropy Constant in Magnetite Nanoparticles. *J. Korean Phys. Soc.* **2011**, *59*, 3069-3073.
48. Mørup, S.; Tronc, E. Superparamagnetic Relaxation of Weakly Interacting Particles. *Phys. Rev. Lett.* **1994**, *72* (20), 3278–3281.
49. Jönsson, P. E.; García-Palacios, J. L. Relaxation Time of Weakly Interacting Superparamagnets. *Europhys. Lett.* **2001**, *55* (3), 418–424.
50. Luis, F.; Petroff, F.; Torres, J. M.; García, L. M.; Bartolomé, J.; Carrey, J.; Vaurès, A. Magnetic Relaxation of Interacting Co Clusters: Crossover from Two- to Three-Dimensional Lattices. *Phys. Rev. Lett.* **2002**, *88* (21), 2172051–2172054.
51. Dormann, J.L.; Bessais, L.; Fiorani, D. A dynamic study of small interacting particles: superparamagnetic model and spin-glass laws *J. Phys. C: Solid State Phys.* **1988**, *21,* 2015-2034.
52. Batlle, X.; Labarta, A. Finite-Size Effects in Fine Particles: Magnetic and Transport Properties *J. Phys. D: Appl. Phys.*, **2002**, *35,* R15–R42.
53. Iglesias, O.; Labarta, A. Magnetic Field Scaling of Relaxation Curves in Small Particle Systems. *J. Appl. Phys.* **2002**, *91*, 4409–4417.